Wave Motion 111 (2022) 102914

Contents lists available at ScienceDirect

Wave Motion

journal homepage: www.elsevier.com/locate/wamot

High-order SAFE computation of reflection and transmission coefficients for functionally-graded poroelastic plates

Vu-Hieu Nguyen [*], Fakharaddin Seyfaddini, Salah Naili

Univ Paris Est Creteil, Univ Gustave Eiffel, CNRS, UMR 8208, MSME, F-94010 Créteil, France

A R T I C L E   I N F O

Article history:
Received 7 July 2021
Received in revised form 3 February 2022
Accepted 28 February 2022
Available online 4 April 2022

Keywords:
Poroelastic waveguide
Functionally graded
Semi-Analytical Finite Element (SAFE)
Spectral element
NURBS
Ultrasound
Bone

A B S T R A C T

This paper aims at studying the ultrasound response of a functionally-graded and anisotropic porous elastic layer surrounded by a fluid in the frequency domain. Based on Biot's theory in a planar configuration, a semi-analytical high-order finite element method was proposed for computing the reflection and transmission coefficients of a plane wave with oblique incidence to the interface between the fluid and poroelastic layer. Two approximation techniques were investigated: (i) spectral element approximation; and (ii) isogeometric approximation. A numerical study was performed on the ultrasound response of bone materials with different depth-varied profiles of porosity showing high effectiveness of the proposed high-order methods.

1. Introduction

Study of the reflection and transmission (R/T) of waves at interfaces of porous waveguides has received much of attention in the past. This attention is motivated by the characterization and optimization problems of the mechanical properties of unknown materials and complex material systems. In many applications, the macroscopic material properties of the studied waveguides are relatively homogeneous along with its longitudinal direction but heterogeneous (with functionally graded or layered profiles) in the cross-section plane. Different analytical and numerical methods have been used to study the wave propagation in its functionally-graded/layered waveguides. For multilayered systems, the semi-analytical techniques such as the Transfer Matrix method (TMM) have often been used [1,2]. By using this method, the wave fields in each horizontal homogeneous layer are analytically decomposed into downward and upward wave components. The wave propagation in the layered medium is then performed through interface operators which are derived from boundary conditions at the upper and lower interfaces of the layers. The use of interface operators is also convenient for considering multiphysics systems such as coupled fluid/elastic/poroelastic media. When the material properties are not piecewise-constant as in layered media but continuously vary, the asymptotic formulation using Peano's series has been developed [3–5]. Although the proposed analytical method is rigorously derived and very fast, it has been shown that numerical instabilities may occur due to positive exponential terms for the cases of large layer thickness (in compared with wavelengths in the medium), requiring some particular techniques [6,7].

The numerical technique called Semi-Analytical Finite Element (SAFE) method [8–11], also known as the Hybrid Numerical Method (HNM, see *e.g.* [12,13]) or Spectral Finite Element Method (SFEM, see *e.g.* [14,15]), has also been widely employed for studying the dispersion of guided waves and the R/T coefficients in prismatic structures with

---

[*] Corresponding author.
E-mail address: vu-hieu.nguyen@u-pec.fr (V.-H. Nguyen).

https://doi.org/10.1016/j.wavemoti.2022.102914
0165-2125/© 2022 Elsevier B.V. All rights reserved.

inhomogeneous properties and/or arbitrary cross-section's geometry. The key point of this method consists in using a hybrid algorithm which begins by employing the Fourier transform (with respect to time and to the longitudinal direction of the waveguide) to transform the problem into the frequency–wavenumber domain. Then, the spectral wave equations are governed in the cross-section plane (or a 1D domain for infinite plates or cylindrical tubes) and may be solved by using the finite element (FE) method [12,15,16]. By using the SAFE method, inhomogeneous material properties in the guided-wave's cross-section may be taken into account without difficulties. Recently, the SAFE method has also been employed in the context of wave propagation in porous waveguides. Liu et al. [17] used this method to obtain the dispersion relations of a multilayer panel which consists of an isotropic poroelastic core sandwiched between two elastic layers. In the same vein, a SAFE procedure for the simulation of the time-domain wave propagation in an anisotropic poroelastic plate immersed in fluids has been developed in [18]. In compared with the finite element method, the SAFE method allows us to gain some significant advantages in terms of memory requirement or computational time. However, as the discretization size needs to be extensively refined when considering strongly heterogeneous cross-section or/and at high frequencies, the computation cost of SAFE method could become significant. For inversion and optimization problems of poroelastic structures [19–21] in which the computational cost is important, there is a necessity to improve the effectiveness of SAFE method for the direct computation of the acoustic response of the considered medium.

This work aims at studying the effectiveness of high-order finite elements within the SAFE framework for the computation of reflection/transmission coefficients of a fluid-saturated poroelastic plate with arbitrary porosity immersed in fluids. To do so, we have investigated and compared two kinds of high-order elements. First, we employed the spectral element technique in which the nodes are located at Gauss–Lobatto–Legendre (GLL) points. Second, isogeometric approximation based on Non-uniform rational basis splines (NURBS) was used. Note that both the spectral element method (SEM) and the isogeometric analysis (IGA) have proved to have great advantages for computation of the wave propagation in different acoustic, viscoelastic or poroelastic waveguides [22–25]. In particular, it has been shown in a recent work [26] that semi-analytical isogeometric finite element method can solve very efficiently the complex eigenvalue problems that allow us to determine the dispersion curves of the phase velocity and attenuation of guided wave in poroelastic plates. As the SAFE computation of R/T coefficients does not deal with solving eigenvalue problems but linear systems of equations, the convergence of isogeometric solutions of R/T waves needs to be carefully studied. Additionally, to the best of the authors' knowledge, the effectiveness of spectral elements in estimation of R/T coefficients of functionally-graded poroelastic plates has not been investigated in the literature. Therefore, a detailed study of both mentioned techniques aiming at estimations R/T coefficients merits interest.

The paper is organized as follows. Section 2 reviews the governing equations for modeling a poroelastic plate immersed in fluids under excitation of an incident plane wave. The Biot theory is used to model the anisotropic poroelastic material. Section 3 presents the finite element formulations with two kinds of shape functions to solve the considered problem. The validation of proposed procedure and numerical examples are presented in Section 4. Section 5 sets out some conclusions. Finally, we provide procedure for analytically estimating the reflection/transmission coefficients of a homogeneous poroelastic plate in Appendix A and the formulations for determination of poroelastic parameters by using a continuum micro-mechanics model in Appendix B.

2. Governing equations

2.1. Problem description

Fig. 1 presents the two-dimensional geometrical description of a poroelastic layer with constant thickness h, which occupies the unbounded domain Ω^b in $\mathbf{e}_1$-axis, is surrounded by two fluid half-spaces Ω_1^f and Ω_2^f. The interfaces between the poroelastic layer Ω^b and the two fluid domains Ω_1^f and Ω_2^f are assumed to be flat and denoted by Γ_1^{bf} and Γ_2^{bf}, respectively.

The surrounding fluids in the domains Ω_1^f and Ω_2^f are assumed to be homogeneous and inviscid. The layer Ω^b is assumed to be a fluid-saturated transversely isotropic poroelastic medium. We also assume that the material properties of the poroelastic layer are homogeneous along with its longitudinal direction, given by $\mathbf{e}_1$-axis, but may be inhomogeneous in its depth direction, given by $\mathbf{e}_2$-axis. Despite the fact that the fluid viscosity is neglected in the surrounding fluid domains, it is taken into account in the porous plate pores. A plane and harmonic wave with an angular frequency ω, propagating in the upper fluid domain, is incident under angle θ_I to the interface Γ_1^{bf}. To determine the reflection and transmission coefficients of the poroelastic layer, we assume a time-dependence $\exp(-\mathrm{i}\omega t)$ (where $\mathrm{i} = \sqrt{-1}$) for all movement quantities $Y(\boldsymbol{x}, t)$, *i.e.* $Y(\boldsymbol{x}, t) = y(\boldsymbol{x}, \omega) \exp(-\mathrm{i}\omega t)$.

In what follows, the term ω in $y(\boldsymbol{x}, \omega)$ will be omitted for simplification and brevity purposes. Moreover, the summation convention over repeated indices is used and the subscript indices after comma stand for the partial derivatives with respect to the space.

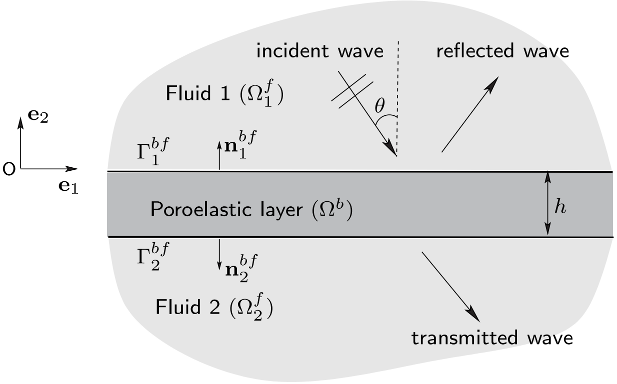

Fig. 1. Geometry description of the poroelastic layer surrounded by two fluid half-spaces.

2.2. Wave propagation in the fluids of domains Ω_1^f and Ω_2^f

The mass densities of fluids in domains Ω_1^f and Ω_2^f are respectively denoted by ρ_1 and ρ_2. The wave celerity in the fluids are respectively denoted by c_1 and c_2. The Helmholtz and Euler equations describing the fluid motion in these domains read:

$$-\frac{\omega^2}{c_n^2}p^{(n)} - p^{(n)}_{,jj} = 0, \tag{1}$$

$$-\omega^2 u_j^{(n)} + \frac{1}{\rho_n}\, p^{(n)}_{,j} = 0, \tag{2}$$

where $p^{(n)}$ and $u_j^{(n)}$ denote respectively the pressure and components of displacement vector of the fluid in Ω_n^f $(n = 1, 2)$.

Let us consider an incident plane and harmonic wave p_I propagating with an angular frequency ω in the upper fluid domain Ω_1^f and arriving at the interface Γ_1^{bf} from an angle θ_I (see Fig. 1). The wavenumber vector of the field p_I may be expressed by $\boldsymbol{k}_I = k_0\boldsymbol{n}_I$ where $k_0 = \omega/c_1$ is the wavenumber and $\boldsymbol{n}_I = (\sin\theta_I, -\cos\theta_I)^T$ is the propagation direction. In the domain Ω_1^f, the pressure field p_I should satisfy the relation (1) and thus has the form given by:

$$p_I = P_I \exp(\mathrm{i}(k_1 x_1 - k_2^{(1)} x_2)), \tag{3}$$

where P_I denotes the wave amplitude, k_1 and $-k_2^{(1)}$ are the projections of the wavenumber vector $\boldsymbol{k}_I$ on $\mathbf{e}_1$-axis and $\mathbf{e}_2$-axis, respectively, and are given by $k_1 = k_0 \sin\theta_I$ and $k_2^{(1)} = k_0\cos\theta_I$. Under the excitation of p_I, the total pressure field in Ω_1^f may be expressed as a superposition of the incident and reflected wave fields:

$$p^{(1)} = p_I + p_R, \tag{4}$$

where p_R is the reflected wave field which may be shown to have the form:

$$p_R = P_R \exp(\mathrm{i}(k_1 x_1 + k_2^{(1)} x_2)), \tag{5}$$

where P_R denotes the reflected wave amplitude. Similarly, the solution of the transmitted wave field in the domain Ω_2^f reads:

$$p^{(2)} = P_T \exp(\mathrm{i}(k_1 x_1 - k_2^{(2)}(x_2 + h))), \tag{6}$$

where P_T denotes the amplitude of the transmitted wave and $-k_2^{(2)}$ is the projection of the wavenumber vector $\boldsymbol{k}^{(2)}$ on $\mathbf{e}_2$-axis: $k_2^{(2)} = \sqrt{(\omega/c_2)^2 - k_1^2}$

2.3. Wave propagation in the anisotropic poroelastic layer Ω^b

Neglecting the body forces (other than inertia), the equations describing the wave propagation in the anisotropic poroelastic layer in the frequency domain read:

$$\sigma_{jk,k} = -\omega^2 \rho\, u_j - \omega^2 \rho_f\, w_j\,, \tag{7}$$

$$-p_{,j} = -\omega^2 \rho_f\, u_j - \omega^2 \tilde{a}_{jk} w_k\,, \tag{8}$$

where $\rho = \phi\, \rho_f + (1-\phi)\, \rho_s$ is the effective mass density where ρ_s and ρ_f denote the solid skeleton and fluid mass densities, respectively; $\tilde{a}_{ij}$ are the components of a frequency-dependent viscodynamic tensor which depends on the permeability and tortuosity of the medium. For a transversely isotropic poroelastic material, $\tilde{\boldsymbol{a}}$ is a diagonal tensor in which $\tilde{a}_{jj},\ j = 1, 2$, is the dynamic tortuosity in $\mathbf{e}_1$- and $\mathbf{e}_2$-axis and is estimated *via* the relation [27,28]:

$$\tilde{a}_{jj}(\omega) = \frac{\rho_f}{\phi}\left(a_j^{\infty} + \frac{\mathrm{i}\phi\eta F_j(\omega)}{\omega\rho_f\kappa_{jj}}\right) \tag{9}$$

where a_j^{∞} is the static tortuosity, η is the dynamic viscosity of the interstitial fluid, κ_{jj} is the intrinsic permeability in $\mathbf{e}_j$-axis; $F_j(\omega)$ is a correction factor which is introduced to take into account the viscous resistance of the fluid flow at high frequencies. We recall that all mechanical characteristics above are x_2-dependent functions. The constitutive equations for an anisotropic poroelastic material are given by:

$$\sigma_{jk} = C_{jklm}\epsilon_{lm} - \alpha_{jk}\, p\,, \tag{10}$$

$$-\frac{1}{M}\, p = w_{j,j} + \alpha_{jk}\epsilon_{jk}\,, \tag{11}$$

where σ_{jk} denote the components of the total stress tensor; ϵ_{jk} denote the components of the strain tensor given by the relation $\epsilon_{jk} = \frac{1}{2}(u_{j,k} + u_{k,j})$ where u_j are components of the solid skeleton's displacement vector; w_j are the fluid/solid relative displacement components weighted by the porosity given by $w_j = \phi(u_j - u_j^f)$ where u_j^f denote the fluid displacement components and ϕ denotes the porosity; C_{jklm} are the components of the elasticity fourth-order tensor of the drained skeleton; α_{jk} are the Biot effective coefficients and M is the Biot's modulus.

For the subsequent mathematical development, we rewrite the equations below in a matrix form. Let us then use Voigt's notation which expresses the symmetric second-order tensors as vectors, so the stress is denoted by $\boldsymbol{s} = (\sigma_{11}, \sigma_{22}, \sigma_{12})^T$, the strain by $\boldsymbol{e} = (\epsilon_{11}, \epsilon_{22}, 2\epsilon_{12})^T$, the Biot effective coefficients by $\breve{\boldsymbol{\alpha}} = (\alpha_{11}, \alpha_{22}, \alpha_{12})^T$ where the superscript $(\star)^T$ designates the transpose operator. We also introduce an operator $\mathbb{L}$ which takes the form:

$$\mathbb{L} = \mathbf{L}_1\partial_1 + \mathbf{L}_2\partial_2, \text{ with } \mathbf{L}_1 = \begin{bmatrix} 1 & 0 \\ 0 & 0 \\ 0 & 1 \end{bmatrix}, \ \mathbf{L}_2 = \begin{bmatrix} 0 & 0 \\ 0 & 1 \\ 1 & 0 \end{bmatrix}, \tag{12}$$

where ∂_1 and ∂_2 denote the partial derivatives with respect to x_1 and x_2, respectively. Using these notations, the equations of linear momentum (7)–(8) may be rewritten as:

$$-\omega^2\rho\, \boldsymbol{u} - \omega^2\rho_f\boldsymbol{w} - \mathbb{L}^T\boldsymbol{s} = \mathbf{0}, \tag{13}$$

$$-\omega^2\rho_f\boldsymbol{u} - \omega^2\tilde{\boldsymbol{a}}\ \boldsymbol{w} + \mathbb{L}^T\boldsymbol{m}\, p = \mathbf{0}, \tag{14}$$

where $\boldsymbol{m} = (1, 1, 0)^T$. The constitutive equations (10)–(11) read:

$$\boldsymbol{s} = \mathbf{C}\,\boldsymbol{e} - \breve{\boldsymbol{\alpha}}\ p, \tag{15}$$

$$p = -M\left(\boldsymbol{m}^T\,\mathbb{L}\,\boldsymbol{w} + \breve{\boldsymbol{\alpha}}^T\mathbb{L}\boldsymbol{u}\right), \tag{16}$$

where $\mathbf{C}$ is the 3-by-3 matrix of the drained elastic tensor written in the Voigt's notation. By noting that $\boldsymbol{e} = \mathbb{L}\boldsymbol{u}$ and by substituting (16) into (15), the constitutive Eqs. (15)–(16) may be written as:

$$\boldsymbol{s} = \mathbf{C}_u\mathbb{L}\boldsymbol{u} + \mathbf{C}_\alpha\mathbb{L}\boldsymbol{w}, \tag{17}$$

$$\boldsymbol{m}p = -\left(\mathbf{C}_M\mathbb{L}\boldsymbol{w} + \mathbf{C}_\alpha^T\mathbb{L}\boldsymbol{u}\right), \tag{18}$$

where the quantities $\mathbf{C}_u, \mathbf{C}_\alpha$ and $\mathbf{C}_M$ are defined as: $\mathbf{C}_u = \mathbf{C} + M\,\breve{\boldsymbol{\alpha}}\,\breve{\boldsymbol{\alpha}}^T, \mathbf{C}_\alpha = M\,\breve{\boldsymbol{\alpha}}\,\boldsymbol{m}^T,\ \mathbf{C}_M = M\,\boldsymbol{m}\,\boldsymbol{m}^T$. The matrix $\mathbf{C}_u$ is known as the undrained elasticity which represents the rigidity of an equivalent elastic medium in which the relative movement between the interstitial fluid and solid skeleton has vanished (*i.e.* when $\boldsymbol{w} = \mathbf{0}$). Note that while $\mathbf{C}_u$ and $\mathbf{C}_M$ are symmetric, $\mathbf{C}_\alpha$ is not. The unsymmetric form of $\mathbf{C}_\alpha$ is due to the anisotropy of the poroelastic medium.

By considering the plane wave nature of presented problem, the solutions of (13) and (14) may be taken under the harmonic form: $y(x_1, x_2) = \hat{y}(k_1, x_2)\, \exp(\mathrm{i}k_1x_1)$. Noting that the operator $\mathbb{L}$ now becomes $\mathbb{L} = \mathrm{i}k_1\mathbf{L}_1 + \partial_2\mathbf{L}_2$, one has:

$$-\omega^2\mathbf{A}_1\mathbf{v} + k_1^2\mathbf{A}_2\mathbf{v} - \mathrm{i}k_1\mathbf{A}_3\partial_2\mathbf{v} - \partial_2\mathbb{t} = \mathbf{0}, \tag{19}$$

where

$$\mathbf{v} = \begin{pmatrix} \hat{\boldsymbol{u}} \\ \hat{\boldsymbol{w}} \end{pmatrix}, \ \mathbb{t} = \begin{pmatrix} \mathbf{L}_2^T\hat{\boldsymbol{s}} \\ -\mathbf{L}_2^T\boldsymbol{m}\hat{p} \end{pmatrix} = ik_1\mathbf{A}_3^T\mathbf{v} + \mathbf{A}_4\partial_2\mathbf{v}, \tag{20}$$

and

$$\mathbf{A}_1 = \begin{bmatrix} \rho\mathbf{1} & \rho_f\mathbf{1} \\ \rho_f\mathbf{1} & \tilde{\boldsymbol{a}} \end{bmatrix}, \quad \mathbf{A}_2 = \begin{bmatrix} \mathbf{C}_u^{11} & \mathbf{C}_\alpha^{11} \\ (\mathbf{C}_\alpha^{11})^T & \mathbf{C}_M^{11} \end{bmatrix}, \tag{21a}$$

$$\mathbf{A}_3 = \begin{bmatrix} \mathbf{C}_u^{12} & \mathbf{C}_\alpha^{12} \\ \left(\mathbf{C}_\alpha^{21}\right)^T & \mathbf{C}_M^{12} \end{bmatrix}, \quad \mathbf{A}_4 = \begin{bmatrix} \mathbf{C}_u^{22} & \mathbf{C}_\alpha^{22} \\ \left(\mathbf{C}_\alpha^{22}\right)^T & \mathbf{C}_M^{22} \end{bmatrix}, \tag{21b}$$

in which $\mathbf{1}$ denotes the 2-by-2 identity matrix; the 2-by-2 matrices $\mathbf{C}_u^{ab}, \mathbf{C}_\alpha^{ab}$ and $\mathbf{C}_M^{ab}$ $(a, b = 1, 2)$ are defined by: $\mathbf{C}_u^{ab} = \mathbf{L}_a^T\mathbf{C}_u\mathbf{L}_b,\ \mathbf{C}_\alpha^{ab} = \mathbf{L}_a^T\mathbf{C}_\alpha\mathbf{L}_b,\ \mathbf{C}_M^{ab} = \mathbf{L}_a^T\mathbf{C}_M\mathbf{L}_b$. One may notice that while matrices $\mathbf{A}_1, \mathbf{A}_2$ and $\mathbf{A}_4$ are symmetric, matrix $\mathbf{A}_3$ is not because of the unsymmetrical form of $\mathbf{C}_\alpha$.

2.4. Interface conditions

At the interfaces Γ_1^{bf} and Γ_2^{bf}, the continuity of pressure and stress fields between the poroelastic medium and the fluid domains requires:

$$p = p^{(n)}, \quad \forall \boldsymbol{x} \in \Gamma_n^{bf}\ (n = 1, 2), \tag{22a}$$

$$\boldsymbol{\sigma}\boldsymbol{n}_n^{bf} = -p^{(n)}\boldsymbol{n}_n^{bf}, \quad \forall \boldsymbol{x} \in \Gamma_n^{bf}\ (n = 1, 2), \tag{22b}$$

where $\boldsymbol{n}_n^{bf}$ is the normal unit vector to Γ_n^{bf} pointing from the poroelastic domain Ω^b toward the fluid domain Ω_n^f (see Fig. 1). In addition, the open-pore condition at the interfaces Γ_n^{bf} $(n = 1, 2)$ is assumed, requiring the continuity of fluid displacement in normal direction (see Eq. (2)):

$$\left(\frac{1}{\rho_n}\nabla p^{(n)} - \omega^2(\boldsymbol{w} + \boldsymbol{u})\right) \cdot \boldsymbol{n}_n^{bf} = 0, \quad \forall \boldsymbol{x} \in \Gamma_n^{bf}. \tag{23}$$

By using the harmonic forms of the solutions defined by $p^{(n)} = \hat{p}^{(n)} \exp(ik_1x_1)$ and by noting that the normal unit vectors of Ω^b at two interfaces Γ_1^{bf} and Γ_2^{bf} (see Fig. 1) are defined by: $\boldsymbol{n}_1^{bf} = -\boldsymbol{n}_2^{bf} = \{0, 1\}^T$, the interface conditions may be expressed as follows:

$$\hat{u}_2 + \hat{w}_2 = \frac{1}{\rho_n\omega^2}\,\partial_2\hat{p}^{(n)}, \quad \forall \boldsymbol{x} \in \Gamma_n^{bf}\ (n = 1, 2), \tag{24a}$$

$$\hat{p} = \hat{p}^{(n)}, \quad \forall \boldsymbol{x} \in \Gamma_n^{bf}\ (n = 1, 2), \tag{24b}$$

$$\hat{\boldsymbol{t}} = \{\, 0, -\hat{p}^{(n)}\}^T, \quad \forall \boldsymbol{x} \in \Gamma_n^{bf}\ (n = 1, 2), \tag{24c}$$

where $\hat{\boldsymbol{t}}$ is the traction vector and is defined by $\hat{\boldsymbol{t}} = \mathbf{L}_2^T\hat{\boldsymbol{s}} = \{\hat{\sigma}_{12}, \hat{\sigma}_{22}\}^T$.

3. Finite element formulation

3.1. Weak formulation

The weak formulation of the boundary value problem given by Eq. (19) and the boundary conditions (24a)–(24c) may be now carried out by using an usual procedure. Let $\mathscr{C}^{ad}$ be the set of admissible functions constituted by the sufficiently differentiable complex-valued functions such as: $x_2 \in H^b = \,]-h, 0[\, \rightarrow \delta\mathbf{v}(x_2) \in \mathbb{C}^4$ where $\mathbb{C}$ is the set of complex numbers. Upon multiplying (19) by a test vector function $\delta\mathbf{v}$ and applying the Gauss theorem, then using the boundary condition (24c), the weak formulation of Eq. (19) reads:

$$\begin{aligned} &-\omega^2\int_{-h}^{0}\delta\mathbf{v}^*\mathbf{A}_1\mathbf{v}\,dx_2 + k_1^2\int_{-h}^{0}\delta\mathbf{v}^*\mathbf{A}_2\mathbf{v}\,dx_2 + ik_1\int_{-h}^{0}\left(\partial_2(\delta\mathbf{v}^*)\mathbf{A}_3^T\mathbf{v} - \delta\mathbf{v}^*\mathbf{A}_3\partial_2\mathbf{v}\right)\,dx_2 \\ &+\int_{-h}^{0}\partial_2(\delta\mathbf{v}^*)\mathbf{A}_4\partial_2\mathbf{v}\,dx_2 + \ \delta\mathbf{v}^*(0)\mathbf{d}\,\hat{p}(0) - \delta\mathbf{v}^*(-h)\mathbf{d}\,\hat{p}(-h) = 0, \forall\ \delta\mathbf{v} \in \mathscr{C}^{ad}, \end{aligned} \tag{25}$$

where $\delta\mathbf{v}^*$ denotes the conjugate transpose of $\delta\mathbf{v}$ and $\mathbf{d} = (0, 1, 0, 1)^T$.

In the weak formulation given by Eq. (25), the pore pressure $\hat{p}$ at $x_2 = 0$ and at $x_2 = -h$ are unknowns but may be determined in terms of the displacement by using the conditions (24a)–(24b) and by taking into account the forms of the general solution in fluid domains presented in Appendix A. At the upper interface between Ω^b and Ω_1^f $(x_2 = 0)$, we have:

$$\hat{u}_2 + \hat{w}_2 = \frac{ik_2^{(1)}}{\rho_1\omega^2}(-P_I + P_R), \tag{26a}$$

$$\hat{p} = P_I + P_R, \tag{26b}$$

which leads to an impedance boundary condition:

$$\hat{p}(0) = \frac{\rho_1\omega^2}{ik_2^{(1)}}(\hat{u}_2(0) + \hat{w}_2(0)) + 2P_I. \tag{27}$$

Similarly the impedance boundary condition at the lower interface ($x_2 = -h$) reads:

$$\hat{p}(-h) = -\frac{\rho_2\omega^2}{ik_2^{(2)}}(\hat{u}_2(-h) + \hat{w}_2(-h)). \tag{28}$$

By noting that $\hat{u}_2 + \hat{w}_2 = \mathbf{d}^T\mathbf{v}$ and by substituting (27)–(28) into (25), we obtain:

$$\begin{aligned} &-\omega^2 \int_{-h}^{0} \delta\mathbf{v}^*\mathbf{A}_1\mathbf{v}\, dx_2 + k_1^2 \int_{-h}^{0} \delta\mathbf{v}^*\mathbf{A}_2\mathbf{v} dx_2 + \mathrm{i}k_1 \int_{-h}^{0} \left(\partial_2(\delta\mathbf{v}^*)\mathbf{A}_3^T\mathbf{v} - \delta\mathbf{v}^*\mathbf{A}_3\partial_2\mathbf{v}\right)\, dx_2 \\ &+ \int_{-h}^{0} \partial_2(\delta\mathbf{v}^*)\mathbf{A}_4\partial_2\mathbf{v} dx_2 + \delta\mathbf{v}^*(0)\mathbf{D}\mathbf{v}(0) + \delta\mathbf{v}^*(-h)\mathbf{D}\mathbf{v}(-h) = -2P_I\delta\mathbf{v}^*(0)\mathbf{d},\ \forall\delta\mathbf{v} \in \mathscr{C}^{ad}, \end{aligned} \tag{29}$$

where $\mathbf{D} = \mathbf{d}\mathbf{d}^T$.

3.2. Finite element discretization

The domain $[-h, 0]$ is discretized into n^{el} elements: $[-h, 0] = \bigcup_e \Omega_e$ with $e = 1, \dots, n^{el}$. By mapping each element Ω_e to the reference domain $\bar{\Omega}_e = [-1, 1]$, the ith component of $\mathbf{v}$ is approximated by:

$$v_i^e = \sum_{j=1}^{q} N_j(\xi)v_i^e(\xi_j), \tag{30}$$

where q is the number of nodes used for this approximation, $N_j(\xi)$ is the jth shape function, ξ_j is the position of jth node and $v_i^e(\xi_j)$ is the nodal solution at jth node. Using the standard Galerkin method, the test function of δv_i^e is approximated by the same shape function. These approximations may be expressed as follows:

$$\mathbf{v}(\xi) = \mathbf{N}^e(\xi)\mathbf{V}^e, \quad \delta\mathbf{v}(\xi) = \mathbf{N}^e(\xi)\delta\mathbf{V}^e, \tag{31}$$

where $\mathbf{N}^e$ is the interpolation matrix constructed from 1D shape functions given by Eq. (30), $\mathbf{V}^e$ and $\delta\mathbf{V}^e$ are the vectors of nodal solutions of $\mathbf{v}$ and $\delta\mathbf{v}$ within the element Ω_e, respectively.

Substituting (31) into (29) and assembling the elementary matrices leads to a system of linear equations:

$$\left(\mathbf{K}^b + \mathbf{K}^\Gamma\right)\mathbf{V} = \mathbf{F}, \tag{32}$$

where $\mathbf{V}$ is the global nodal solution vector; $\mathbf{K}^b$ is the global "stiffness matrix" of the poroelastic layer; $\mathbf{K}_\Gamma$ represents the coupling operator between the fluid and poroelastic layers; the vector $\mathbf{F}$ is the external force vector due to the incident waves. Note that the element number of the vectors $\mathbf{V}$ and $\mathbf{F}$ is $n = 4(n^{el} \times q - 1)$ because each node has 4 degrees of freedom. Thus, the sizes of $\mathbf{K}^b$ and $\mathbf{K}^\Gamma$ equal to $n \times n$ and are defined by:

$$\mathbf{K}^b = -\omega^2\, \mathbf{K}_1 + k_1^2\, \mathbf{K}_2 + ik_1\, \mathbf{K}_3 + \mathbf{K}_4 \tag{33a}$$

$$\mathbf{K}^\Gamma_{jk} = \begin{cases} \dfrac{\rho_2\omega^2}{ik_2^{(2)}} & \text{if } (j,k) = (2,2), (2,4), (4,2), (4,4) \\ \dfrac{\rho_1\omega^2}{ik_2^{(1)}} & \text{if } (j,k) = (n-2, n-2),\ (n-2, n), \\ & \qquad (n, n-2),\ (n, n) \\ 0 & \text{otherwise} \end{cases} \tag{33b}$$

$$\mathbf{F}_j = \begin{cases} -2P_I & \text{if } j = n-2, n \\ 0 & \text{otherwise} \end{cases} \tag{33c}$$

where the matrices $\mathbf{K}_1, \mathbf{K}_2, \mathbf{K}_3$ and $\mathbf{K}_4$ are defined by:

$$\mathbf{K}_1 = \bigcup_e \int_{-1}^{1} \left(\mathbf{N}^e(\xi)\right)^T \mathbf{A}_1(\xi)\mathbf{N}^e(\xi)\mathcal{J}(\xi)\, d\xi, \tag{34a}$$

$$\mathbf{K}_2 = \bigcup_e \int_{-1}^{1} \left(\mathbf{N}^e(\xi)\right)^T \mathbf{A}_2(\xi)\mathbf{N}^e(\xi)\mathcal{J}(\xi)\, d\xi, \tag{34b}$$

$$\mathbf{K}_3 = \bigcup_e \int_{-1}^{1} 2\left[\left(\partial_2\mathbf{N}^e(\xi)\right)^T \mathbf{A}_3(\xi)\mathbf{N}^e(\xi)\right]_a d\xi, \tag{34c}$$

$$\mathbf{K}_4 = \bigcup_e \int_{-1}^{1} \left(\partial_2\mathbf{N}^e(\xi)\right)^T \mathbf{A}_4(\xi)\left(\partial_2\mathbf{N}^e(\xi)\right)\mathcal{J}^{-1}(\xi)\, d\xi, \tag{34d}$$

in which $\mathcal{J}$ is the Jacobian operator and $[\star]_a$ designates the anti-symmetric part of $[\star]$.

By using the standard finite element method (FEM) to solve Eq. (29), the elements' size of the spatial discretization has to be sufficiently refined, *i.e.* a sufficient number of grid points per wavelength has to be adjusted, to be able to capture the oscillation of the solution. Thus, the quality of numerical solutions depends on the wave-number k_1. When solving a Helmholtz-type equation, the rule that must be respected is that the ratio $k_1\ell^e$ must be constant where ℓ^e is the element size. However, as shown in studies on the error bound estimation when the FEM is used for solving Helmholtz equation, as k_1 increases, the accuracy of FE solution still significantly decreases while the ratio $k_1\ell^e$ is kept to be constant, due to the so-called "pollution effect". It has also been shown that for large wave-number problems, using high-order interpolation polynomials would be better to reduce the pollution effect than use lower-order ones with refined element sizes. To do so, we propose to use two different high-order approximation techniques: the first one uses the spectral element method (SEM) and the second one uses the isogeometric analysis (IGA) method.

3.3. On the use of high-order spectral-elements

The high-order spectral-element method (SEM) has been widely used for wave propagation simulation (see *e.g.* [29]). Like standard FEM, the SEM uses the Lagrange polynomials as interpolation functions. In the reference element $[-1, 1]$, one may define q Lagrange polynomials of degree $(q-1)$ based on q-nodes ξ_i (for $-1 \leq \xi_i \leq 1$):

$$N_j^{q-1}(\xi) = \prod_{i=1, i\neq j}^{q} \frac{(\xi - \xi_i)}{(\xi_j - \xi_i)}, \tag{35}$$

which imposes the condition given by $N_j^{q-1}(\xi_i) = \delta_{ij}$ where δ_{ij} denote the Kronecker symbol for which $\delta_{ij} = 1$ if $i = j$ else $\delta_{ij} = 0$ if $i \neq j$. One important difference between FEM and SEM is the node distribution within an element. In SEM, the coordinates of nodes are chosen to be located at the q Gauss–Lobatto–Legendre (GLL) points which are the roots of the following equation:

$$(1 - \xi^2)P'_{q-1}(\xi) = 0, \tag{36}$$

where $P'_{q-1}(\xi)$ denotes the first-order derivative of the Legendre polynomial of degree $(q-1)$ with respect to ξ. It is worth noting that in the time-domain simulation, this choice is motivated by the fact that the mass matrix will become a diagonal matrix which is very convenient for employing an explicit time integration scheme.

3.4. On the use of NURBS basis functions

In the framework of the SAFE approach, we consider the non-uniform rational B-spline (NURBS) basis functions [25,30] for discretization of the weak problem presented in Section 3.1. A two-dimensional plate only needs to be described by one-dimensional NURBS curve elements. The NURBS are defined from B-spline. In a parametric approach, B-spline basis functions of order q are constructed using a sequence of non-decreasing set of coordinates called *knot vector* defined as $\Xi = \{\xi_1, \xi_2, \xi_3, \ldots, \xi_{n+q+1}\}$, where $\xi_i \in \mathbb{R}$ (where $\mathbb{R}$ denotes the set of real numbers and $i = 1, 2, \ldots, n$) is the ith knot and n is the number of basis functions used to construct the B-spline curve. The B-spline basis functions $B_{i,q}$ can be defined recursively by:

$$q = 0 \;:\quad B_{i,0}(\xi) = \begin{cases} 1 & \text{if } \xi_i < \xi < \xi_{i+1}, \\ 0 & \text{otherwise}, \end{cases} \tag{37a}$$

$$q > 0 \;:\quad B_{i,q}(\xi) = \frac{(\xi - \xi_i)}{(\xi_{i+q} - \xi_i)} B_{i,q-1}(\xi) + \frac{(\xi_{i+q+1} - \xi)}{(\xi_{i+q+1} - \xi_{i+1})} B_{i+1,q-1}(\xi). \tag{37b}$$

NURBS basis functions $N_{i,q}(\xi)$ can be defined by assigning a weight w_i to every B-spline function $B_{i,q}(\xi)$:

$$N_{i,q}(\xi) = \frac{B_{i,q}(\xi) w_i}{\sum_{j=1}^{n} B_{j,q}(\xi) w_j}. \tag{38}$$

3.5. Reflection and transmission coefficients

By solving the linear system of Eqs. (32), one obtains the displacement at all the nodes. Then, the reflection and transmission coefficients, denoted R and T respectively, can be computed by using the displacement values at the upper and the lower surfaces, respectively (see Eqs. (26a) and (28)):

$$R = \frac{P_R}{P_I} = \frac{\rho_1 \omega^2}{i k_2^{(1)}} \times \frac{\hat{u}_2(0) + \hat{w}_2(0)}{P_I} + 1, \tag{39a}$$

$$T = \frac{P_T}{P_I} = -\frac{\rho_2 \omega^2}{i k_2^{(2)}} \times \frac{\hat{u}_2(-h) + \hat{w}_2(-h)}{P_I}. \tag{39b}$$

Table 1
Values of the parameters for cortical bone.

Mass density of the fluid ρ_f	1000	kg.m^{-3}
Bulk modulus of the fluid K_f	2.25	GPa
Mass density of the solid ρ_s	1722	kg.m^{-3}
Young's modulus of the solid E_s	20	GPa
Poisson's coefficient of the solid ν_s	0.3	–
Viscosity of the fluid η	10^{-3}	Pa.s
Characteristic length in $\boldsymbol{e}_1$-direction Λ_1	2	µm
Characteristic length in $\boldsymbol{e}_2$-direction Λ_2	0.2	µm
Tortuosity in a_1^∞-direction $\boldsymbol{e}_1$	1	–
Tortuosity in a_2^∞-direction $\boldsymbol{e}_2$	1	–

Table 2
Parameters of poroelastic materials with different porosities.

ϕ [−]	C_{11} [GPa]	C_{22} [GPa]	C_{12} [GPa]	C_{66} [GPa]	α_{11} [−]	α_{22} [−]	M [GPa]	κ_{11} [m^{-2}]	κ_{22} [m^{-2}]
0.05	26.668	20.252	8.452	6.294	0.1083	0.1463	35.574	2.5×10^{-12}	2.5×10^{-14}
0.5	12.672	5.708	2.327	1.865	0.6605	0.765	4.1941	2.5×10^{-11}	2.5×10^{-13}

4. Numerical results

4.1. Material parameters

As an example of the capability of the method presented, we have studied the effect of porosity on the dynamic response of cortical bone while using ultrasound diagnostic devices. Many of the past studies have focused on the modeling of guided waves in long bones by using fluid-loaded homogeneous/multilayer/functional graded plate models. The understanding of wave phenomena involved in the long bone structures has been studied by many authors in the frequency-domain [3,31] or in the time-domain [32–34]. In these studies, the cortical bone material has been considered as an equivalent (visco-)elastic medium of which the effective macroscopic mass density and effective macroscopic elasticity tensor are estimated from its porosity. The presence of the interstitial fluid, which was considered in many works for the analysis of the behavior of cortical bone (*e.g.* [35–37]) or of ultrasonic wave propagation through cancellous bones (*e.g.* [38–41]), has usually been neglected when studying ultrasonic wave propagation in cortical bones.

The observations at all ages and for both genders show that the mean porosity in the endosteal region (inner part of the bone) is significantly higher than the porosity in the periosteal region (outer part of the bone) [42]. This observation may be explained by the fact that the cortical bone is affected by age-related bone resorption and osteoporosis, causing reduction of bone shell thickness as well as an increase in porosity, namely in the endosteal region. Moreover, the macroscopic mechanical properties of bones have proved to strongly depend on their porosity [43,44]. As a consequence, the cortical bone may naturally be considered as a functionally graded material.

In this study, both surround fluid domains Ω_1^f and Ω_2^f are also assumed to be the water with the mass densities and wave celerities given by $\rho_1 = \rho_2 = 1000$ kg.m^{-3} and $c_1 = c_2 = 1500$ m.s^{-1}, respectively. The material properties and the pore geometry of the poroelastic plate are determined by assuming that the solid skeleton is an isotropic elastic material and the pores have a cylindrical shape. Here, the poroelastic constants (see Eqs. (10)–(11), $\mathbf{C}$, $\boldsymbol{\alpha}$ and M) are determined following a micro-mechanical approach presented in [45]. Moreover, the permeability is calculated depending on the porosity, the pore surface area and the cross section parameters by using the Kozeny–Carman law (see details in [46]). In all the examples that follow, the solid and fluid phases' parameters are fixed as shown in Table 1 and only the porosity ϕ varies. The poroelastic constants are determined for each value of ϕ. For example, Table 2 shows the numerical values of the poroelastic constants computed for $\phi = 0.05$ and $\phi = 0.5$, respectively.

4.2. Cases of homogeneous poroelastic plates

4.2.1. Reference solutions

We first consider a homogeneous anisotropic poroelastic bone plate with thickness $h = 5$ mm immersed in water for which the analytical solutions may be determined using the procedure described in Appendix A. For illustration purposes, we present in Figs. 2(a,b) the variation of the coefficient R as a function of the incidence angle θ at two frequencies ($f = 0.25$ MHz and $f = 1$ MHz). For each frequency, the graphs of $|R(\theta)|$ of plates with different porosities ($\phi = 0.01, 0.05, 0.2, 0.5$) are shown. When ϕ is very small (case of $\phi = 0.01$, shown by solid black curves), the poroelastic plate behaves similarly to an elastic plate. On the other hand, when ϕ increases, the behavior of a poroelastic plate is very different from an elastic plate. Note that the reflection coefficient R gets the minimum values (close to zero) at some angles of incidence corresponding to the guided-wave modes of which the phase velocities are given by $C_{ph} = c_1/\sin\theta$ [47]. For example, when $f = 250$ kHz (see Fig. 2a), three zero-peaks found at $\theta \sim 12.5°$, $25°$ and $51.5°$ correspond to the A_1, S_0 and

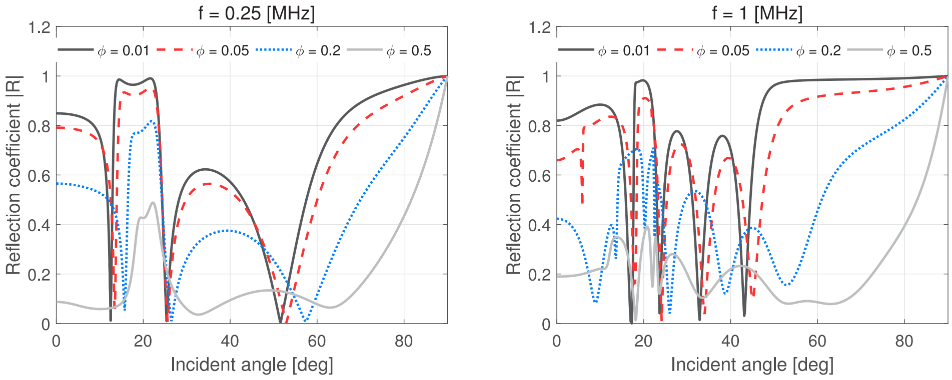

(a) $f = 250$ kHz (b) $f = 1$ MHz

Fig. 2. Reflection coefficient $|R|$ *versus* incident angle θ for a homogeneous plate.

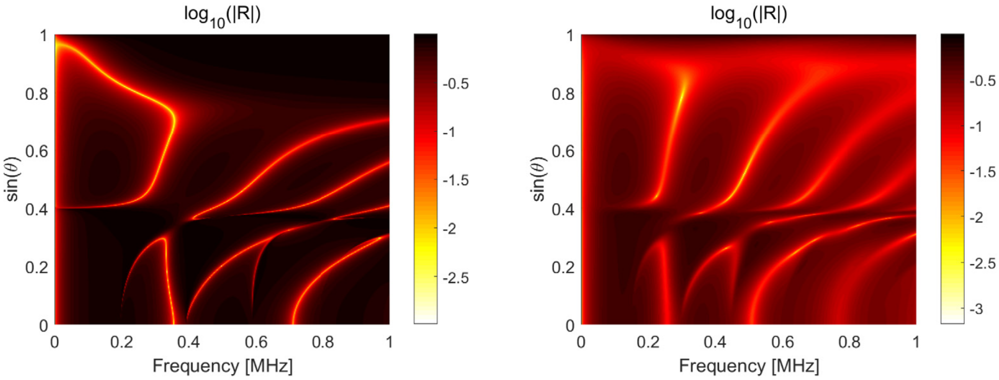

(a) $\phi = 0.05$ (b) $\phi = 0.5$

Fig. 3. Case of homogeneous plates: reflection coefficient $|R|$ *versus* incident angle (θ) and frequency ($f = \omega/2\pi$).

A_0 modes, respectively. At a high frequency ($f = 1$ MHz), as the plate's thickness is important compared with the incident wavelength, there exists a critical angle ($\theta \sim 50°$) above which the incident plane wave is nearly totally reflected (see Fig. 2b). By increasing the porosity ϕ, both elasticity and absorption of the poroelastic material are accordingly changed, causing significant modifications not only in the amplitudes of reflected waves but also in the phase velocity of the modes. This effect is more pronounced at a high frequency. For higher porosity, when the stiffness of the plate is smaller than the one of the precedent case, we may check that the reflection coefficient has globally smaller values.

In Fig. 3, we present the variation of modulus of $|R|$ with respect to both incident angle θ and the frequency f in two cases of porosity $\phi = 0.05$ and $\phi = 0.5$. As it would be expected, a greater number of modes may be observed for the plate with $\phi = 0.5$ than the one with $\phi = 0.05$ in a same frequency range [0, 1] MHz.

4.2.2. Validation

To validate the proposed numerical methods, we have investigated the reflection and transmission coefficients (R and T, respectively) obtained for $f = 1$ MHz with various incident angles as shown in Fig. 4. As the plate is homogeneous, the reflection and transmission coefficients can be analytically calculated (see Appendix A) and are served as reference solutions. Three finite element solutions are shown in this figure. The first one has been obtained by using the standard SAFE method with 6 quadratic Lagrange elements ($p = 2$). The second one has been computed by using only one high-order spectral GLL element with $p = 12$. The third one has been obtained by one NURBS-based element with $p = 12$. As a consequence, all of these three FE meshes contain in total 13 nodes with 52 degrees of freedom. At the studied frequency ($f = 1$ MHz), both real and imaginary parts of R and T solutions obtained by using the high-order elements (GLL or NURBS) perfectly match the analytical ones for all values of θ. On the contrary, the $R-$ and $T-$curves computed by using low-order elements ($p = 2$) have proved to significantly be less accurate, namely for the small incident angle values between 0° and 20°. In particular, some lack precision at some incident angles. For example, the peaks of both reflection and transmission coefficients at the incident angle $\theta \sim 6°$ displayed in zoomed windows have proved not to be precisely evaluated when using the standard quadratic elements.

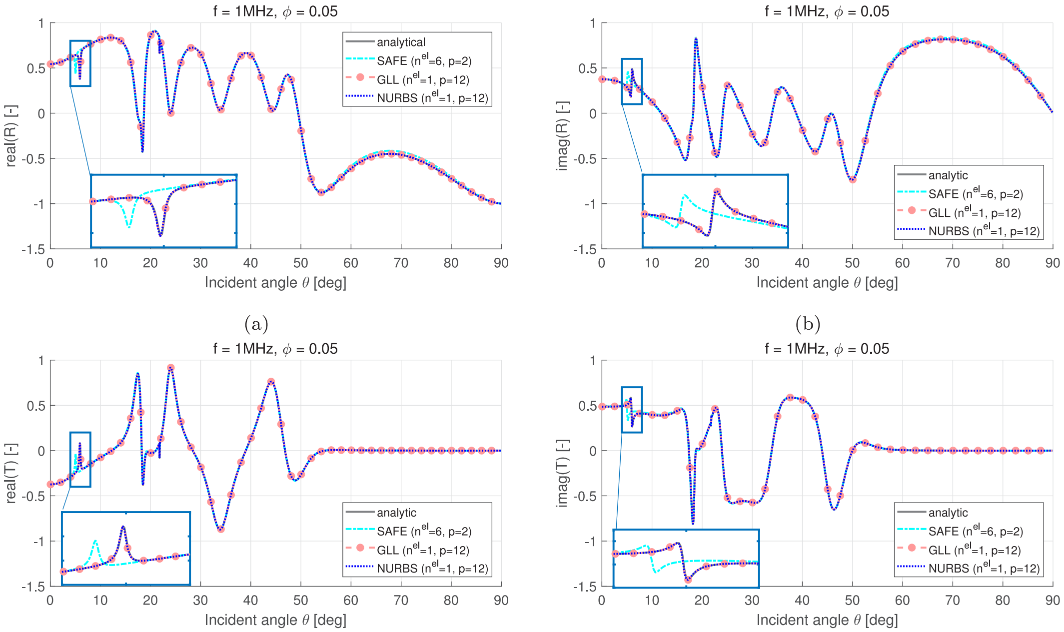

(a) (b)

(c) (d)

Fig. 4. Exact and FE solutions of the refection and transmission coefficients *versus* incident angle θ.

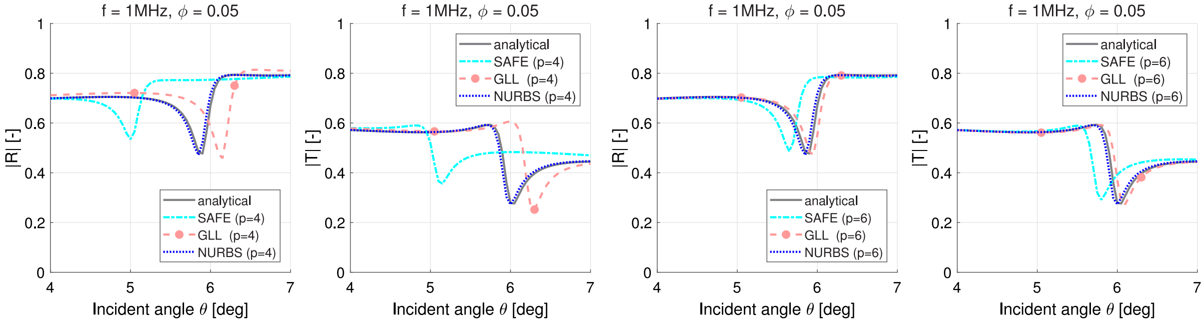

(a) $p = 4$ (b) $p = 6$

Fig. 5. Exact and FE solutions of the refection and transmission coefficients computed with $p = 4$ and $p = 6$.

In Figs. 5(a,b), we present the R- and $T-$ solutions of the same problem computed by employing two different orders of interpolation functions ($p = 4$ and $p = 6$) but by keeping the same total number of degrees of freedoms to be 52 as the one used in the previous analysis with $p = 12$. To clarify the comparison between different solutions, we focused on the peak found at $\theta \sim 6°$. It could be observed that the solutions computed using NURBS-based shape functions are correctly approached, even when using $p = 4$ for which both standard SAFE and GLL solutions led to inaccurate results. Using $p = 6$ seems to allow improving remarkably the accuracy of solutions computed by using Lagrange elements.

Next, we examine the case of a bone plate with the same thickness but with a higher porosity ($\phi = 0.5$) whose poroelastic properties are given in Table 2. As the porosity is higher, the material's stiffness decreases and the permeability increases. Again, the FE solutions were computed by using six quadratic elements (standard SAFE) or one 12th-order element (GLL or NURBS) when $f = 1$ MHz. The obtained numerical solutions of $|R|$ and of $|T|$ were compared to the analytical ones as shown in Fig. 6. The results obtained with quadratic elements were shown to have a significant difference with respect to the analytical solution. The errors of both R and T seem to be more significant than the ones obtained when $\phi = 0.05$ (see Fig. 5. On the contrary, the solutions obtained with only one 12th-order GLL element still match very well the analytical ones (see Figs. 6a). Interestingly, using NURBS-based shape function with $p = 2$ leads to a much more accurate estimation of R and T (see Figs. 6b).

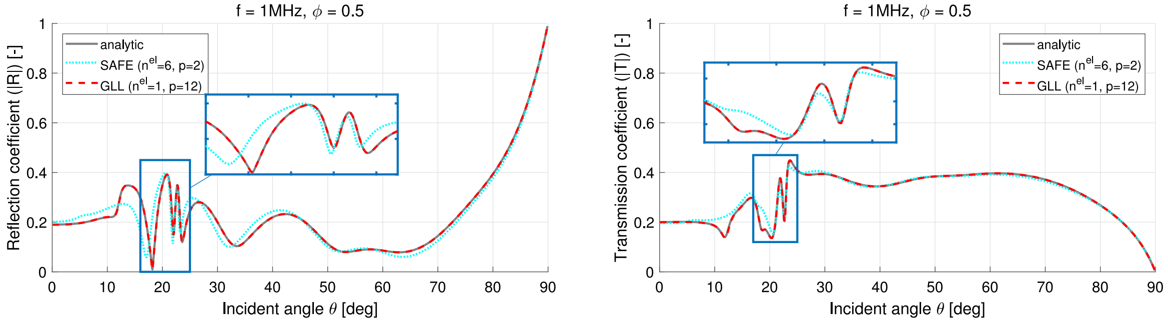

(a) solutions using SAFE and GLL

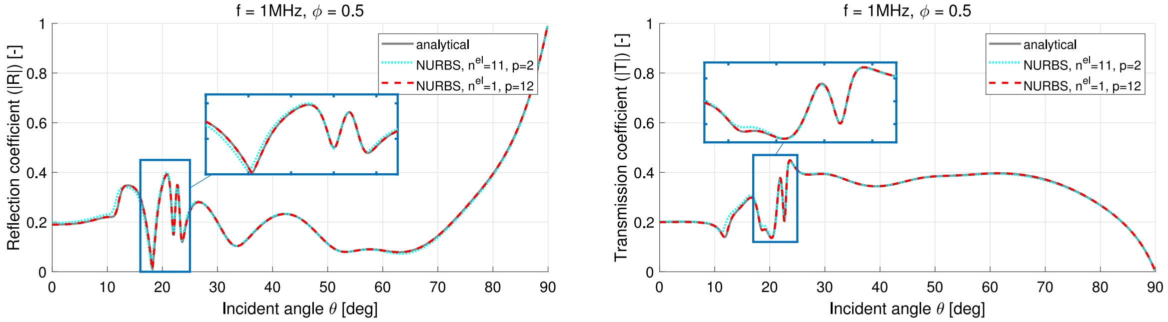

(b) solutions using NURBS

Fig. 6. Homogeneous plate with $\phi = 0.5$: Exact and FE solutions of the refection and transmission coefficients *versus* the incident angle θ.

4.2.3. Convergence study

The later examples show that the use of high-order GLL or NURBS elements may significantly reduce the numerical errors when computing the reflection and transmission coefficients. In order to examine this feature in more detail, we performed a convergence study of R and T computed with different interpolation function's orders p. For estimating the error, we introduced a function E^{refl} which is defined as a the mean value of the relative error estimated over the range of incident angles from 0° to 90°:

$$E^{\text{refl}} = \left(\frac{1}{n^\theta} \sum_{i=1}^{n^\theta} \left| \frac{R^{\text{FE}}(\theta_i) - R^{\text{exact}}(\theta_i)}{R^{\text{exact}}(\theta_i)} \right|^2 \right)^{\frac{1}{2}}, \tag{40}$$

where n^θ is the number of incident value considered. In Fig. 7, the relative error on R with respect to the total number of nodes is presented in a logarithmic scale. In Fig. 7(a) and (b), we depict the error obtained by using GLL elements (spectral element method) or NURBS elements (isogeometric analysis), respectively. For both methods, the computations were performed with $p = 2$, $p = 4$, $p = 8$, $p = 10$ and $p = 12$.

Regarding the use of GLL elements (see Fig. 7(a)), one may notice that by using lower-order elements ($p = 2, 4$) the slopes of the error curves are much smaller than the ones obtained with the high-order elements ($p = 8, 10, 12$). For a same total number of nodes ($n^{\text{node}} = 25$), while the mesh based on two elements with $p = 12$ leads to an error of order 10^{-6}, the one based on 9 elements with $p = 4$ leads to an error of order 10^{-2}. Thus, using high-order elements ($p = 12$) could allow us to improve significantly the accuracy of the estimations R and T compared with the results obtained with $p = 2$ or $p = 4$. However, the accuracy gains are not so significant if we compare the results obtained with $p = 8$, $p = 10$ and $p = 12$, even the one obtained with $p = 12$ is still the best.

When using NURBS-base shape functions (see Fig. 7(b)), further increasing the order p more than 8 does not lead to a significant improvement of the convergence, similarly to the previous remark on the use of GLL elements. However, the convergence could be achieved much faster by using NURBS. For example, in the case $p = 4$, while using GLL elements required a mesh of 25 nodes to get $E(R) \sim 10^{-3}$, using IGA only requires a mesh with only 15 nodes (control points) to achieve the same precision. This advantage feature may be explained by the fact that by using NURBS, C^1-continuity condition was always fulfilled over the domain $\bar{\Omega} = [-h, 0]$.

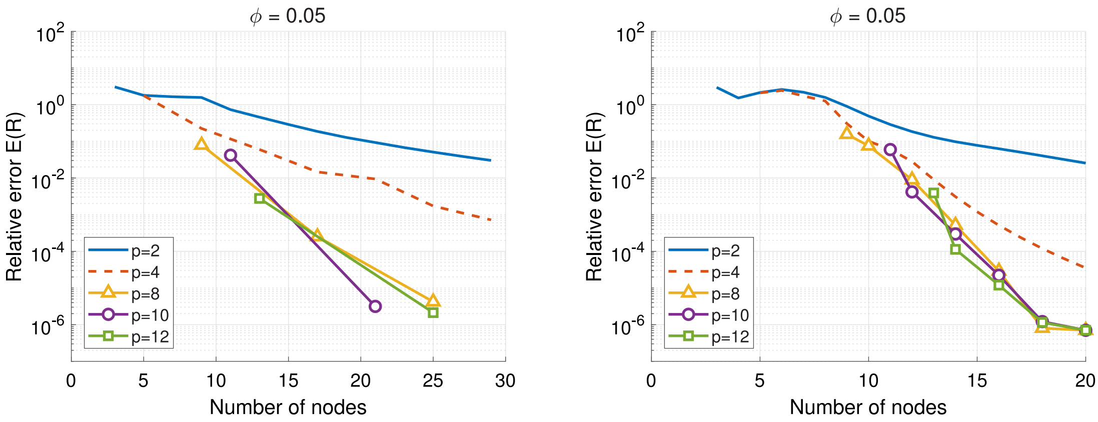

(a) spectral elements　(b) isogeometric

Fig. 7. Error of reflection and transmission coefficients *versus* the total number of nodes.

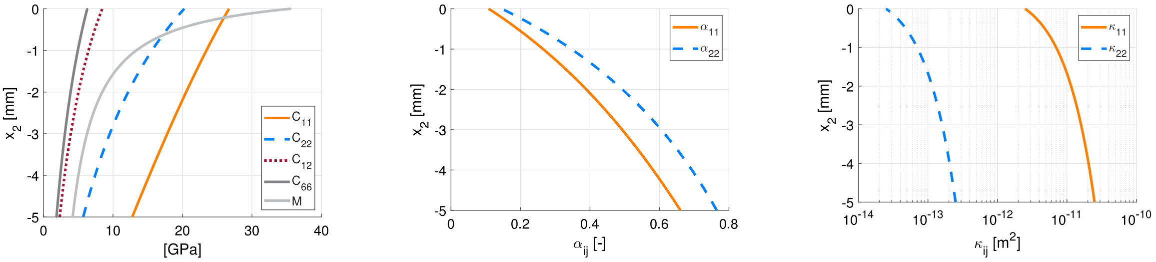

(a) C_{ij} and M　(b) α_{ij}　(c) κ_{ij}

Fig. 8. Profile of poroelastic properties with respect to the depth-coordinate x_2.

4.3. Cases of poroelastic plates with linear gradient of porosity

In this section, the bone plate has a functionally-graded porosity variation. To do so, the porosity at the upper surface is fixed at the value $\phi_1 = 0.05$. A linear-gradient of porosity is defined by giving a value ϕ_2 at the lower surface as follows:

$$\phi(x_2) = \frac{1}{h}(\phi_1 - \phi_2)x_2 + \phi_1. \tag{41}$$

Then, one can estimate the physical parameters of the poroelastic material depending on the depth-coordinate x_2 following the procedure presented in Appendix B. For example, Fig. 8 depicts the profiles of the components of the elasticity tensor (given in Voigt notation C_{ij}), the Biot coefficients (α_{ij}, M) and the permeability κ_{ij}.

As it can be observed in Fig. 9 in which the cases $\phi_2 = 0.2$, $\phi_2 = 0.5$ and $\phi_2 = 0.8$ are considered, the reflection coefficient is shown to strongly depend, not only on the porosity at the upper surface, but also on the gradient of the porosity in the in-depth direction. Moreover, this effect is more significant in the high frequency range. In Fig. 10, the graphs of R versus θ computed at two frequencies given at $f = 0.25$ MHz and $f = 1$ MHz are plotted. At each frequency, the comparison between the homogeneous case $\phi_2 = 0.05$ and the linear gradient cases ($\phi_2 = 0.2$, $\phi_2 = 0.5$) confirms that at a low frequency ($f = 0.25$ MHz), the porosity gradient slightly affects the behavior of the reflection coefficient R. The minima's locations of the case $\phi = 0.5$ are nearly unchanged compared with the homogeneous plate case. However, the graphs of $R(\theta)$ are completely changed when regarding a higher frequency ($f = 1$ MHz) for which the wavelengths are shorter and are more sensitive to the porosity variation.

The convergence study has also been carried out for these functionally-graded poroelastic plates in order to check the performance of the proposed numerical methods. Similarly to the convergence study previously performed for the homogeneous plate (see Section 4.2.3), in Figs. 11(a) and (b), numerical errors obtained by using GLL and NURBS-based discretizations, respectively, are presented. As exact solutions are not available for the functionally-graded cases, standard SAFE solutions using overkill meshes are served as the reference solutions. Once again, using high-order shape functions ($p \geq 8$) for both methods has proved to be efficient to reduce the numerical errors. Moreover, the IGA solutions have proved to be converged faster than the ones computed by using GLL discretization.

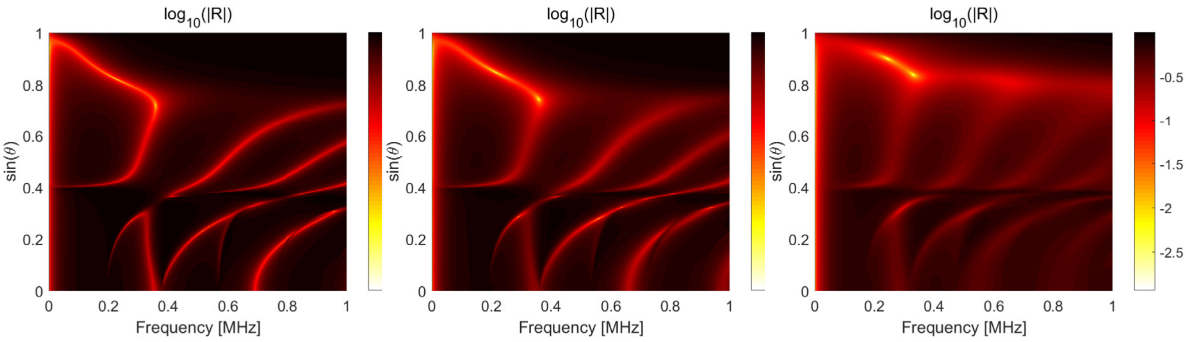

(a) $\phi_2 = 0.2$ (b) $\phi_2 = 0.5$ (c) $\phi_2 = 0.8$

Fig. 9. Reflection coefficient $|R|$ *versus* θ and f for functionally-graded plates ($\phi_1 = 0.05$).

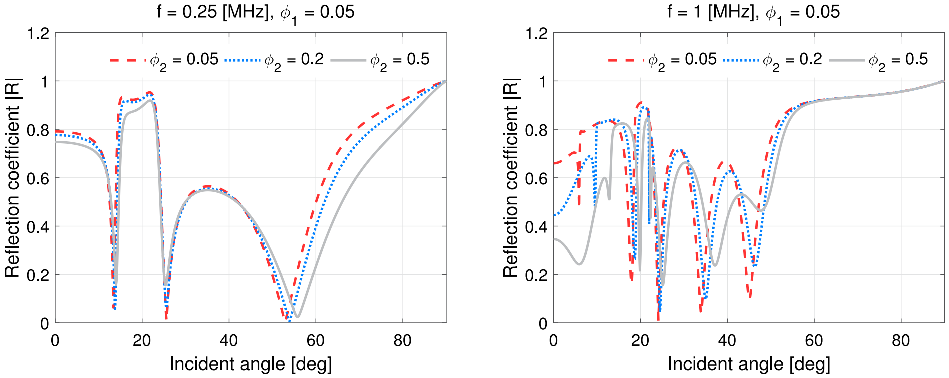

Fig. 10. Reflection coefficient $|R|$ *versus* incident angle θ: influence of a porosity gradient.

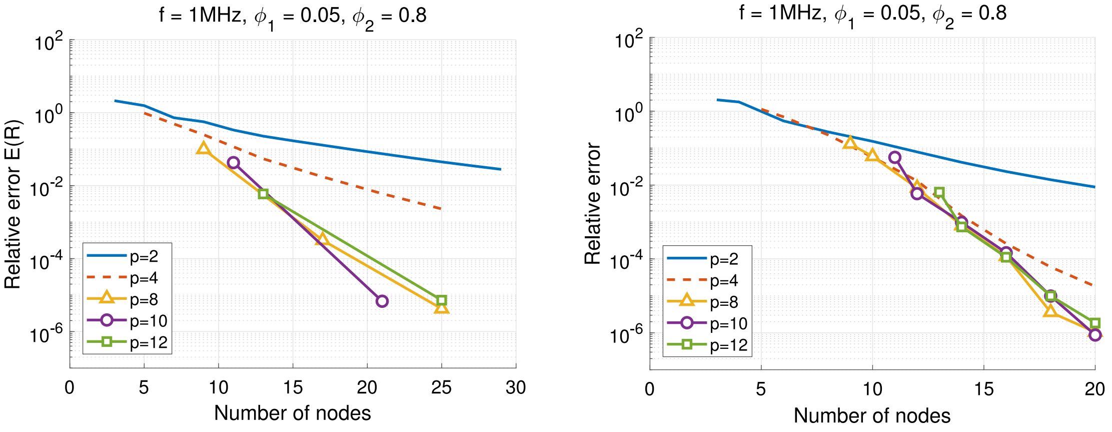

(a) spectral elements   (b) isogeometric

Fig. 11. Case of a functionally-graded-porosity plate: Error on reflection and transmission coefficients *versus* the total number of nodes.

5. Conclusion

In this paper, an approach based on the semi-analytical high-order finite element method is proposed for the determination of the reflection and transmission coefficients of a two-dimensional poroelastic waveguide wherein the material properties could be heterogeneous and anisotropic. Two strategies have been proposed for the discretization and approximation of solutions: the first one employs the spectral elements based on Gauss–Lobatto-Legendre (GLL) nodes and the second one uses the NURBS-based shape functions. The convergence analysis shows that the standard SAFE method with quadratic Lagrange elements has a relatively slow rate of convergence, especially at the high frequency range. Using high-order elements has proved to be interesting as it allows us to significantly improve the accuracy of numerical solutions of R and T. Both proposed methods were shown to be efficient in this context. Even so, the NURBS-based approximation is likely to lead to faster convergence compared with the one obtained by using spectral element approximations. For the computation, using a spectral element method, the use of elements with an order more than 8 would be recommended to get a significant effectiveness. When using IGA, the use of a NURBS-based shape function with $p = 4$ would be already sufficient to achieve the same accuracy.

It is worth noting that the numerical procedure proposed in this paper is not only limited for long bone ultrasound characterization but also for other applications in acoustical engineering, in which the functionally-graded material properties should be taken into account. For example, the proposed methods could be useful for studies on the acoustic absorption optimization of poroelastic composites [20,21].

CRediT authorship contribution statement

Vu-Hieu Nguyen: Mathematical development/implementation, Concept & design of study, Analysis of results, Writing – review & editing. **Fakharaddin Seyfaddini:** Mathematical development/implementation, Analysis of results, Writing – review & editing. **Salah Naili:** Concept & design of study, Analysis of results, Writing – review & editing.

Declaration of competing interest

The authors declare that they have no known competing financial interests or personal relationships that could have appeared to influence the work reported in this paper.

Appendix A. Analytical solution of reflection and transmission coefficients for a homogeneous layer

If the poroelastic layer is homogeneous, the solution of the system given by Eq. (19) may be analytically derived [48,49]. Here, we present a simple procedure for calculating the analytical solution of reflection and transmission coefficients by using the displacement-based equation (see (19)):

$$-\omega^2\mathbf{A}_1\mathbf{v} + k_1^2\mathbf{A}_2\mathbf{v} - \mathrm{i}k_1\left(\mathbf{A}_3 + \mathbf{A}_3^T\right)\partial_2\mathbf{v} - \mathbf{A}_4\partial_2^2\mathbf{v} = \mathbf{0}. \tag{A.1}$$

Assuming that $\mathbf{v}$ has the form $\mathbf{v} = \mathbf{D}\exp(\gamma x_2)$, where $\mathbf{D}$ and γ are constants to be determined. The condition for a non-trivial solution of Eq. (A.1) leads to a characteristic equation:

$$\mathcal{D}(\gamma) := \det\left(-\omega^2\mathbf{A}_1 + k_1^2\mathbf{A}_2 - \mathrm{i}k_1\gamma\left(\mathbf{A}_3 + \mathbf{A}_3^T\right) + \gamma^2\mathbf{A}_4\right) = 0, \tag{A.2}$$

where det is the determinant operator.

The analytical expression of $\mathcal{D}(\gamma)$ may be found without difficulties with the help of symbolic software. In this paper, Matlab Symbolic Toolbox has been used. It has been shown that although the size of matrices in Eq. (A.1) is 4-by-4, the derived expression for $\mathcal{D}(\gamma)$ is a 6th-order polynomial:

$$\mathcal{D}(\gamma) := b_0\gamma^6 + b_1\gamma^4 + b_2\gamma^2 + b_3, \tag{A.3}$$

where b_j $(j = 0, \ldots, 3)$ are constants. Eq. (A.3) allows us to determine 6 roots γ_j, $(j = 1, \ldots, 6)$ verifying $\gamma_4 = -\gamma_1$, $\gamma_5 = -\gamma_2$, $\gamma_6 = -\gamma_3$ and 6 associated to normalized eigenvectors $\mathbf{B}_j$, $(j = 1, \ldots, 6)$. As a consequence, the general solution $\mathbf{v}$ may be expressed by the linear combination $\mathbf{v} = \sum_{j=1}^{6}\mathbf{D}_j\exp(\gamma_j x_2)$, where $\mathbf{D}_j = A_j\mathbf{B}_j$ $(j = 1, \ldots, 6)$. The quantities A_j are six unknown constants which will be determined by using the boundary conditions. Without loss of generality, we may assume that $\mathrm{Re}(\gamma_j) > 0$ for $j = 1, 2, 3$ where $\mathrm{Re}(\gamma_j)$ stands for the real part of γ_j.

To solve this problem with the boundary conditions given in (24a)–(24c), we first use the solution of $\mathbf{v}$ to calculate the general solutions of concerning displacement and stress components $\hat{u}_1, \hat{u}_2, \hat{w}_2$ and $\hat{\sigma}_{12}, \hat{\sigma}_{22}, \hat{p}$ respectively. Then, by making some algebraic manipulations, we are able to write the general solution of these terms under matrix form as follows:

$$\begin{pmatrix}\bar{\mathbf{v}}\\ \bar{\mathbf{t}}\end{pmatrix} = \begin{bmatrix}\mathbf{B}_{11} & \mathbf{B}_{12}\\ \mathbf{B}_{21} & \mathbf{B}_{22}\end{bmatrix}\begin{bmatrix}\mathbf{e}^- & \mathbf{0}\\ \mathbf{0} & \mathbf{e}^+\end{bmatrix}\begin{pmatrix}\mathbf{A}^-\\ \mathbf{A}^+\end{pmatrix}, \tag{A.4}$$

where $\bar{\mathbf{v}} = (\hat{u}_1, \hat{u}_2, \hat{w}_2)^T$, $\bar{\mathbf{t}} = (\hat{\sigma}_{12}, \hat{\sigma}_{22}, -\hat{p})^T$, $\mathbf{B}_{11}, \mathbf{B}_{12}, \mathbf{B}_{21}$ and $\mathbf{B}_{22}$ are the 3-by-3 matrices which are extracted from $\mathbf{D}_j$ (see Eq. (20)). The quantities $\mathbf{e}^+$ and $\mathbf{e}^-$ are defined by:

$$\mathbf{e}^+ = \mathrm{diag}(\exp\gamma_1x_2, \exp\gamma_2x_2, \exp\gamma_3x_2), \quad \mathbf{e}^- = \mathrm{diag}(\exp-\gamma_1x_2, \exp-\gamma_2x_2, \exp-\gamma_3x_2), \tag{A.5}$$

where $\mathbf{A}^+ = (A_1, A_2, A_3)^T$ and $\mathbf{A}^- = (A_4, A_5, A_6)^T$.

Noting that $\hat{u}_2 + \hat{w}_2 = \bar{\mathbf{d}}^T\bar{\mathbf{v}}$ with $\bar{\mathbf{d}} = (0, 1, 1)^T$, the continuity conditions (see Eq. (24a)) read:

$$\bar{\mathbf{d}}^T\bar{\mathbf{v}}|_{x_2=0} = \frac{ik_2^{(1)}}{\rho_1\omega^2}(P_I - P_R), \quad \bar{\mathbf{t}}|_{x_2=0} = -\bar{\mathbf{d}}(P_I + P_R), \tag{A.6a}$$

$$\bar{\mathbf{d}}^T \bar{\mathbf{v}}|_{x_2=-h} = -\frac{ik_2^{(2)}}{\rho_2 \omega^2} P_T, \quad \bar{\mathbf{t}}|_{x_2=-h} = -\bar{\mathbf{d}} P_T \tag{A.6b}$$

which becomes

$$\beta^{(1)} P_R + \bar{\mathbf{d}}^T \mathbf{B}_{11} \mathbf{A}^- + \bar{\mathbf{d}}^T \mathbf{B}_{12} \mathbf{A}^+ = \alpha^{(1)} P_I, \tag{A.7a}$$

$$\bar{\mathbf{d}} P_R + \mathbf{B}_{21} \mathbf{A}^- + \mathbf{B}_{22} \mathbf{A}^+ = -\bar{\mathbf{d}} P_I, \tag{A.7b}$$

$$\beta^{(2)} P_T + \bar{\mathbf{d}}^T \mathbf{B}_{11} \mathbf{e}_h^+ \mathbf{A}^- + \bar{\mathbf{d}}^T \mathbf{B}_{12} \mathbf{e}_h^- \mathbf{A}^+ = 0, \tag{A.7c}$$

$$\bar{\mathbf{d}} P_T + \mathbf{B}_{21} \mathbf{e}_h^+ \mathbf{A}^- + \mathbf{B}_{22} \mathbf{e}_h^- \mathbf{A}^+ = \mathbf{0}, \tag{A.7d}$$

where

$$\beta^{(1)} = \frac{\rho_1 \omega^2}{ik_2^{(1)}}, \quad \beta^{(2)} = \frac{\rho_2 \omega^2}{ik_2^{(2)}}, \quad \mathbf{e}_h^+ = \operatorname{diag}(\exp \gamma_1 h, \exp \gamma_2 h, \exp \gamma_3 h), \quad \mathbf{e}_h^- = \left(\mathbf{e}_h^+\right)^{-1}. \tag{A.8}$$

In order to avoid numerical difficulties due to the exponential term with large values of $\mathrm{Re}(\gamma_j)$, we make some arrangements in (A.7a)–(A.7d) to obtain a system of linear equations as follows:

$$\begin{bmatrix} \beta^{(1)} & \bar{\mathbf{d}}^T \mathbf{B}_{11} \mathbf{e}_h^- & \bar{\mathbf{d}}^T \mathbf{B}_{12} \mathbf{e}_h^- & 0 \\ \bar{\mathbf{d}} & \mathbf{B}_{21} \mathbf{e}_h^- & \mathbf{B}_{22} \mathbf{e}_h^- & \mathbf{0} \\ \mathbf{0} & \mathbf{B}_{21} & \mathbf{B}_{22} \mathbf{e}_{2h}^- & \bar{\mathbf{d}} \\ 0 & \bar{\mathbf{d}}^T \mathbf{B}_{11} & \bar{\mathbf{d}}^T \mathbf{B}_{12} \mathbf{e}_{2h}^- & \beta^{(2)} \end{bmatrix} \begin{pmatrix} P_R \\ \mathbf{e}_h^+ \mathbf{A}^- \\ \mathbf{e}_h^+ \mathbf{A}^+ \\ P_T \end{pmatrix} = \begin{pmatrix} \beta^{(1)} P_I \\ -P_I \bar{\mathbf{d}} \\ \mathbf{0} \\ 0 \end{pmatrix}. \tag{A.9}$$

The amplitudes of reflected and transmitted waves P_I and P_R may be obtained by solving the linear system of equations (see Eq. (A.9)). Consequently, the reflection and transmission coefficients may be computed by:

$$R = \frac{P_R}{P_I} \quad \text{and} \quad T = \frac{P_T}{P_I}. \tag{A.10}$$

Appendix B. Determination of poroelastic parameters

To describe the behavior of the poroelastic bone plate, the drained elasticity tensor $\mathbb{C}$ as well as Biot's effective coefficients $\boldsymbol{\alpha}$ and $\boldsymbol{M}$ should be provided. For this study, these parameters are derived from the characteristics of the interstitial fluid and solid skeleton phases by using a continuum micro-mechanics model proposed by Hellmich et al. [45]. According to this model, the micro-pores at the micro-structural scale are regarded as cylindrical pores with a circular cross section. In drained conditions, the constitutive behavior of the material inside the pores does not possess stiffness. Hence, the estimated drained micro-structural stiffness of the bone whose solid bone matrix's elasticity tensor is $\mathbb{C}^m$ reads:

$$\mathbb{C} = (1-\phi)\mathbb{C}^m : \left\{(1-\phi)\mathbb{I} + \phi\left[\mathbb{I} - \mathbb{P}^{cyl} : \mathbb{C}^m\right]^{-1}\right\}^{-1}, \tag{B.1}$$

where $\mathbb{I}$ denotes the fourth-order identity tensor; $\mathbb{P}^{cyl}$ the fourth-order tensor is Hill's tensor for materials with periodical cylindrical inclusions, which may be derived in closed form [45]. The tensor $\boldsymbol{\alpha}$ the constant M can be then evaluated by [50]:

$$\boldsymbol{\alpha} = \mathbf{I} - \mathbb{C} : (\mathbb{S}^m : \mathbf{I}), \qquad -\frac{1}{M} = C - \boldsymbol{\alpha} : \mathbb{S} : \boldsymbol{\alpha}, \tag{B.2}$$

where $\mathbb{S} = (\mathbb{C})^{-1}$ and $\mathbb{S}_m = (\mathbb{C}_m)^{-1}$ are respectively the drained and solid material compliance tensors, I designates the second-order tensor identity and the scalar C denotes the effective compressibility of porous matrix material, which is given by

$$C = \frac{1}{K} - \frac{1}{K_m} + \phi\left(\frac{1}{K_f} - \frac{1}{K_m}\right), \tag{B.3}$$

where $K = (\mathbf{I} : \mathbb{S} : \mathbf{I})^{-1}$, K_f and $K_m = (\mathbf{I} : \mathbb{S}_m : \mathbf{I})^{-1}$ are the bulk *moduli* of the drained porous matrix and of the interstitial fluid and of the poroelastic material, respectively.

References

[1] B. Hosten, M. Castaings, Transfer matrix of multilayered absorbing and anisotropic media. measurements and simulations of ultrasonic wave propagation through composite materials, J. Acoust. Soc. Am. 94 (3) (1993) 1488–1495.

[2] G. Lefeuve-Mesgouez, A. Mesgouez, G. Chiavassa, B. Lombard, Semi-analytical and numerical methods for computing transient waves in 2D acoustic/poroelastic stratified media, Wave Motion 49 (7) (2012) 667–680.

[3] C. Baron, S. Naili, Propagation of elastic waves in a fluid-loaded anisotropic functionally graded waveguide: Application to ultrasound characterization, J. Acoust. Soc. Am. 127 (3) (2010) 1307–1317.

[4] G. Gautier, L. Kelders, J.-P. Groby, O. Dazel, L. De Ryck, P. Leclaire, An application of the Peano series expansion to predict sound propagation in materials with continuous pore stratification, J. Acoust. Soc. Am. 130 (3) (2011) 1390–1398.

[5] A. Geslain, J.-P. Groby, O. Dazel, S. Mahasaranon, K. Horoshenkov, A. Khan, An application of the Peano series expansion to predict sound propagation in materials with continuous pore stratification, J. Acoust. Soc. Am. 132 (1) (2012) 208–215.

[6] O. Dazel, J.-P. Groby, B. Brouard, C. Potel, A stable method to model the acoustic response of multilayered structures, J. Appl. Phys. 113 (8) (2013) 083506–1–083506–10.

[7] J. Jocker, D. Smeulders, G. Drijkoningen, C. van der Lee, A. Kalfsbeek, Matrix propagator method for layered porous media: Analytical expressions and stability criteria, Geophysics 69 (4) (2004) 1071–1081.

[8] F. Treyssede, K.-L. Nguyen, A.-S. Bonnet-BenDhia, C. Hazard, Finite element computation of trapped and leaky elastic waves in open stratified waveguides, Wave Motion 51 (7) (2014) 1093–1107.

[9] V.-H. Nguyen, T.N. Tran, M.D. Sacchi, S. Naili, L.H. Le, Computing dispersion curves of elastic/viscoelastic transversely-isotropic bone plates coupled with soft tissue and marrow using semi-analytical finite element (SAFE) method, Comput. Biol. Med. 87 (2017) 371–381.

[10] D. Pereira, G. Haiat, J. Fernandes, P. Belanger, Simulation of acoustic guided wave propagation in cortical bone using a semi-analytical finite element method, J. Acoust. Soc. Am. 141 (4) (2017) 2538–2547.

[11] P. Zuo, Z. Fan, SAFE-PML approach for modal study of waveguides with arbitrary cross sections immersed in inviscid fluid, J. Sound Vib. 406 (2017) 181–196.

[12] X. Han, G.R. Liu, K.Y. Lam, Transient waves in plates of functionally graded materials, Internat. J. Numer. Methods Engrg. 52 (8) (2001) 851–865.

[13] X. Han, G.R. Liu, Z.C. Xi, K.Y. Lam, Transient waves in a functionally graded cylinder, Int. J. Solids Struct. 38 (17) (2001) 3021–3037.

[14] S. Gopalakrishnan, A. Chakraborty, D. Roy Mahapatra, Spectral Finite Element Method, Springer, 2008.

[15] A. Marzani, Time-transient response for ultrasonic guided waves propagating in damped cylinders, Int. J. Solids Struct. 45 (25–26) (2008) 6347–6368.

[16] C. Desceliers, C. Soize, Q. Grimal, G. Haiat, S. Naili, A time-domain method to solve transient elastic wave propagation in a multilayer medium with a hybrid spectral-finite element space approximation, Wave Motion 45 (4) (2008) 383–399.

[17] H. Liu, S. Finnveden, M. Barbagallo, I. Arteaga, Wave propagation in sandwich panels with a poroelastic core, J. Acoust. Soc. Am. 135 (5) (2014) 2683–2693.

[18] V.-H. Nguyen, S. Naili, Simulation of ultrasonic wave propagation in anisotropic poroelastic bone plate using hybrid spectral/finite element method, Int. J. Numer. Methods Biomed. Eng. 28 (8) (2012) 861–876.

[19] M. Niskanen, A. Duclos, O. Dazel, J.-P. Groby, J. Kaipio, T. Lahivaara, Estimating the material parameters of an inhomogeneous poroelastic plate from ultrasonic measurements in water, J. Acoust. Soc. Am. 146 (4) (2019) 2596–2607, http://dx.doi.org/10.1121/1.5129369.

[20] N. Gorbushin, S. Naili, V.H. Nguyen, Optimizing microstructure of a poroelastic layer with cylindrical pores for absorption properties, Mech. Res. Commun. 102 (2019) 103422.

[21] N. Gorbushin, V.H. Nguyen, S. Naili, Design optimisation of acoustic absorbers with cross-like pores via a homogenisation method, Acta Acust. United Acust. 105 (4) (2019) 638–649.

[22] C. Morency, J. Tromp, Spectral-element simulations of wave propagation in porous media, Geophys. J. Int. 175 (1) (2008) 301–345, http://dx.doi.org/10.1111/j.1365-246X.2008.03907.x.

[23] H. Gravenkamp, S. Natarajan, W. Dornisch, On the use of NURBS-based discretizations in the scaled boundary finite element method for wave propagation problems, Comput. Methods Appl. Mech. Engrg. 315 (2017) 867–880.

[24] Y. Liu, S. Lin, Y. Li, C. Li, Y. Liang, Numerical investigation of Rayleigh waves in layered composite piezoelectric structures using the SIGA-PML approach, Composites B 158 (2019) 230–238.

[25] F. Seyfaddini, H. Nguyen-Xuan, V.-H. Nguyen, A semi-analytical isogeometric analysis for wave dispersion in functionally graded plates immersed in fluids, Acta Mech. 232 (2021) 15–32.

[26] F. Seyfaddini, H. Nguyen-Xuan, V.-H. Nguyen, Semi-analytical IGA-based computation of wave dispersion in fluid-coupled anisotropic poroelastic plates, Int. J. Mech. Sci. 212 (2021) 106830.

[27] D.L. Johnson, J. Koplik, R. Dashen, Theory of dynamic permeability and tortuosity in fluid-saturated porous media, J. Fluid Mech. 176 (1987) 379–402.

[28] V.H. Nguyen, E. Rohan, S. Naili, Multiscale simulation of acoustic waves in homogenized heterogeneous porous media with low and high permeability contrasts, Internat. J. Engrg. Sci. 101 (2016) 92–109.

[29] D. Komatitsch, J.-P. Vilotte, The spectral element method: An efficient tool to simulate the seismic response of 2D and 3D geological structures, Bull. Seismol. Soc. Am. 88 (2) (1998) 368–392.

[30] J.A. Cottrell, T.J. Hughes, Y. Bazilevs, Isogeometric Analysis: Toward Integration of CAD and FEA, John Wiley & Sons, 2009.

[31] C. Baron, S. Naili, Elastic wave propagation in a fluid-loaded anisotropic waveguide with laterally varying properties, Comptes Rendus Mécanique 336 (2008) 722–730.

[32] E. Bossy, M. Talmant, P. Laugier, Effect of bone cortical thickness on velocity measurements using ultrasonic axial transmission: A 2D simulation study, J. Acoust. Soc. Am. 112 (2002) 297–307.

[33] Q. Grimal, S. Naili, A theoretical analysis in the time-domain of wave reflection on a bone plate, J. Sound Vib. 298 (2006) 12–29.

[34] G. Haiat, S. Naili, Q. Grimal, M. Talmant, C. Desceliers, C. Soize, Influence of a gradient of material properties on ultrasonic wave propagation in cortical bone: Application to axial transmission, J. Acoust. Soc. Am. 125 (6) (2009) 4043–4052.

[35] D. Zhang, S. Cowin, Oscillatory bending of a poroelastic beam, J. Mech. Phys. Solids 42 (10) (1994) 1575–1599.

[36] V.-H. Nguyen, T. Lemaire, S. Naili, Influence of interstitial bone microcracks on strain-induced fluid flow, Biomech. Model. Mechanobiol. 10 (6) (2011) 963–972.

[37] C. Baron, V.H. Nguyen, S. Naili, C. Guivier-Curien, Interaction of ultrasound waves with bone remodelling: a multiscale computational study, Biomech. Model. Mechanobiol. 19 (5) (2020) 1755–1764.

[38] J. Williams, Ultrasonic wave propagation in cancellous and cortical bone: prediction of some experimental results by Biot's theory, J. Acoust. Soc. Am. 91 (2) (1992) 1106–1112.

[39] Y. Nagatani, K. Mizuno, T. Saeki, M. Matsukawa, T. Sakaguchi, H. Hosoi, Numerical and experimental study on the wave attenuation in bone - FDTD simulation of ultrasound propagation in cancellous bone, Ultrasonics 48 (6) (2008) 607–612.

[40] V.-H. Nguyen, S. Naili, V. Sansalone, Simulation of ultrasonic wave propagation in anisotropic cancellous bones immersed in fluid, Wave Motion 47 (2) (2010) 117–129.

[41] V.-H. Nguyen, S. Naili, Semi-analytical solution of transient plane waves transmitted through a transversely isotropic poroelastic plate immersed in fluid, J. Eng. Math. 86 (1) (2014) 125–138.

[42] C. Thomas, S. Feik, J. Clement, Regional variation of intracortical porosity in the midshaft of the human femur: age and sex differences, J. Anat. 206 (2005) 115–125.

[43] N.X. Dong, E.X. Guo, The dependence of transverse isotropic elasticity of human femoral cortical boneon porosity, J. Biomech. 37 (8) (2004) 1281–1287.
[44] C. Baron, M. Talmant, P. Laugier, Effect of porosity on effective diagonal stiffness coefficients (c_{ii}) and anisotropy of cortical bone at 1 MHz: A finite difference time domain study, J. Acoust. Soc. Am. 122 (2007) 1810–1817.
[45] C. Hellmich, F.-J. Ulm, Microporodynamics of bones: Prediction of the ''Frenkel-Biot" slow compressional wave, J. Engrg. Mech. 131 (9) (2005) 918–927.
[46] G. Rosi, V.-H. Nguyen, S. Naili, Numerical investigations of ultrasound wave propagating in long bones using a poroelastic model, Math. Mech. Solids 21 (1) (2016) 119–133.
[47] J.L. Rose, Ultrasonic Guided Waves in Solid Media, Cambridge University Press, 2014.
[48] Z. Fellah, J. Chapelon, S. Berger, W. Lauriks, C. Depollier, Ultrasonic wave propagation in human cancellous bone: Application of Biot theory, J. Acoust. Soc. Am. 116 (1) (2004) 61–73.
[49] A. Vashishth, P. Khurana, Waves in stratified anisotropic poroelastic media: a transfer matrix approach, J. Sound Vib. 277 (1–2) (2004) 239–275.
[50] M. Thompson, J. Willis, A reformation of the equations of anisotropic poroelasticity, J. Appl. Mech. ASME 58 (1991) 612–616.